Chemical Science

ROYAL SOCIETY OF CHEMISTRY

EDGE ARTICLE

View Article Online
View Journal

Check for updates

Cite this: DOI: 10.1039/d5sc09992g

All publication charges for this article have been paid for by the Royal Society of Chemistry

Mapping the crystallization landscape of rare earth MOFs: a high-throughput investigation of structure, kinetics, and selectivity

Madeleine A. Gaidimas,[ab] Gyu-Hee Kim,[ab] Zi-Ming Ye,[ab] Julian S. Magdalenski,[ab] Nathaniel M. Barker,[a] Abhijoy Mandal,[c] Kourosh Darvish,[cd] Kent O. Kirlikovali,[ab] Varinia Bernales,[cdef] Alán Aspuru-Guzik,[cdeghijk] Christos D. Malliakas[a] and Omar K. Farha *[ablm]

Systematically exploring the multidimensional parameter space of metal–organic framework (MOF) crystallization remains challenging due to limited adoption of high-throughput (HT), automated experimental workflows. MOF development is dominated by manual synthesis and characterization methods and a trial-and-error approach, and the integration of HT MOF synthesis with HT characterization and analysis is uncommon. Here, we present a practical HT MOF discovery workflow that combines automated solvothermal synthesis with three scalable characterization methods. First, we characterize bulk structure using HT powder X-ray diffraction (PXRD) and rapid matching of PXRD data to reported MOF crystal structures. We also employ a custom machine-learning based computer vision (CV) model to identify MOF formation rates from images of sample vials. Finally, we develop a HT X-ray fluorescence (XRF) method to quantify elemental ratios in bimetallic MOF samples. As a case study, we investigate the crystallization of rare earth (RE) MOFs, systematically probing the effects of reaction conditions such as metal identity, linker structure, temperature, and acid concentration. We then leverage these insights to demonstrate a proof-of-concept selective crystallization from a mixed RE solution. Using our HT workflow, we performed 1488 unique MOF crystallization reactions and characterized the resulting samples through the collection of >800 PXRD patterns, CV analysis of >13 000 images, and elemental analysis measurements of 144 bimetallic crystallization reactions. We identified 5 previously unreported rare earth MOFs (NU-2501–NU-2505) and characterized their structures with single-crystal X-ray diffraction (SCXRD) and microcrystal electron diffraction (MicroED). Our HT approach enabled us to construct phase diagrams mapping out the crystallization preferences and formation kinetics for 18 distinct RE-MOF products. By unifying automated MOF synthesis with multimodal characterization, we demonstrate the efficient exploration of a complex synthetic landscape, generating insights into MOF structure, crystallization kinetics, and composition.

Received 19th December 2025
Accepted 8th June 2026

DOI: 10.1039/d5sc09992g

rsc.li/chemical-science

Introduction

The rise of automated synthesis, data-rich experimentation, and high-throughput (HT) workflows have enabled rapid progress in materials discovery. Despite progress in fields including photovoltaics,[1–3] batteries,[4,5] and catalysis,[6–8] the adoption of these tools towards the synthesis of metal–organic frameworks (MOFs) remains limited. The modular nature of MOFs, which are assembled from inorganic node and organic linker building units, creates a massive combinatorial design space of

---

[a] Department of Chemistry, Northwestern University, Evanston, IL 60208, USA. E-mail: o-farha@northwestern.edu
[b] International Institute for Nanotechnology, Northwestern University, Evanston, IL 60208, USA
[c] Department of Computer Science, University of Toronto, Toronto, ON M5S 2E4, Canada
[d] Acceleration Consortium, Toronto, ON M5S 3H6, Canada
[e] Department of Chemistry, University of Toronto, Toronto, ON M5S 2E4, Canada
[f] Materials Discovery Research Institute, UL Research Institutes, Skokie, IL 60077, USA
[g] Vector Institute for Artificial Intelligence, Toronto, ON M5G 1M1, Canada
[h] Department of Chemical Engineering and Applied Chemistry, University of Toronto, Toronto, ON M5S 3E5, Canada
[i] Department of Materials Science and Engineering, University of Toronto, Toronto, ON M5S 3E4, Canada
[j] Senior Fellow, Canadian Institute for Advanced Research (CIFAR), Toronto, ON M5G 1M1, Canada
[k] NVIDIA, Toronto, ON M5V 1K4, Canada
[l] Department of Chemical and Biological Engineering, Northwestern University, Evanston, IL 60208, USA
[m] Paula M. Trienens Institute for Sustainability and Energy, Northwestern University, Evanston, IL 60208, USA

frameworks with varied topologies and pore geometries.[9,10] However, MOF development remains dominated by low-throughput, trial-and-error approaches to optimize reaction conditions to achieve target materials.[11] Beyond the node and linker building units, a range of additional parameters are crucial to produce phase-pure, high-quality materials, including the synthesis temperature,[12,13] reaction duration,[14,15] stoichiometry,[16] solvents,[17,18] and acid modulators.[19,20] MOF crystallization is often highly sensitive to subtle variations in these conditions. Therefore, identifying the correct synthetic pathway to access a target MOF product is not necessarily straightforward, and novel frameworks are often discovered serendipitously.[21,22] Optimization of synthesis procedures requires further tedious manual experimentation. The difficulty of navigating this complex crystallization landscape necessitates the development of HT workflows for MOF synthesis and characterization.

Previous studies have demonstrated the utility of HT approaches towards MOF reaction condition optimization,[18,23–29] as well as exploratory synthesis campaigns to expedite the discovery of novel frameworks.[30–32] Rapid MOF synthesis can be achieved with automated instruments to expedite reagent addition and sample preparation. However, HT characterization methods are equally important to prevent bottlenecks in a HT MOF workflow. HT MOF characterization has been explored using methods including powder X-ray diffraction (PXRD),[25,28] optical microscopy,[30] electron microscopy,[33] electron diffraction,[34,35] and porosity measurements.[36] Yet workflows combining both HT MOF synthesis and HT MOF characterization remain rare. Additionally, many HT studies are targeted towards the optimization of a specific MOF, limiting their generalizability for future framework discovery.

In this work, we present a HT MOF workflow incorporating both automated synthesis and three HT characterization methods. Our goal was to develop a practical platform to facilitate the systematic exploration of MOF crystallization conditions. First, we use automated synthesis methods to rapidly conduct hundreds of solvothermal MOF synthesis reactions. These syntheses were performed at a conventional exploratory synthesis scale, rather than as miniaturized reactions, enabling direct use of bulk characterization instrumentation. We characterized the crystallinity of the resulting solid products with HT-PXRD and used a custom HT search-match screening tool to identify experimental samples consistent with reported MOF structures. Unmatched samples, representing potentially unreported MOFs, were flagged for further manual characterization by SCXRD and MicroED. To reveal MOF crystallization kinetics, we deployed a custom machine-learning-based computer vision (CV) model to identify solid MOF products from images of sample vials. Finally, we developed a HT X-ray fluorescence (XRF) method to elucidate the elemental composition of mixed-metal MOFs. In combination, these methods provide insight into the structure, kinetics, and selectivity of MOF crystallization (Fig. 1a).

As a proof-of-concept system for our HT synthesis and characterization workflow, we chose to investigate the crystallization of rare earth (RE) MOFs. REs, encompassing the lanthanides, Sc, and Y, can adopt high and flexible coordination numbers.[37] This translates to unique framework topologies and significant diversity in the accessible product MOFs.[38] The ability of REs to form varied framework structures creates a challenging, synthetically diverse landscape, which we considered an ideal testing ground to demonstrate our HT synthesis and characterization capabilities. Rather than relying on individual serendipitous reactions, we embarked on a systematic campaign to map the relationships between synthetic parameters and the resulting RE-MOF structure, kinetics, and composition.

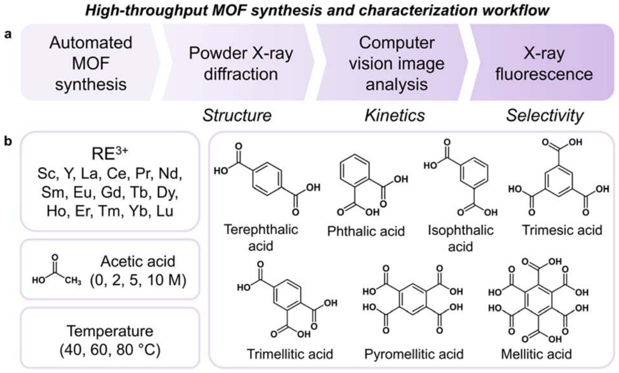

Fig. 1 (a) High-throughput workflow for exploratory MOF synthesis and characterization. (b) Synthetic parameters investigated in the RE-MOF automated synthesis campaign.

Results and discussion

High-throughput MOF synthesis campaign

We selected 16 metals for our HT RE-MOF synthesis campaign, including 14 trivalent lanthanides (La, Ce, Pr, Nd, Sm, Eu, Gd, Tb, Dy, Ho, Er, Tm, Yb, Lu) as well as Sc and Y. The nitrate salts of these metals were crystallized with seven commercially available carboxylate-based organic linkers, including three ditopic linkers (terephthalic acid, phthalic acid, isophthalic acid), two tritopic linkers (trimesic acid, trimellitic acid), one tetratopic linker (pyromellitic acid) and one hexatopic linker (mellitic acid). Our crystallization trials were conducted in a green solvent system consisting of ethanol and water. Additionally, we investigated three synthesis temperatures (40, 60, 80 °C) and four concentrations of acetic acid modulator to identify kinetic and thermodynamic effects in the RE-MOF crystallization landscape. This combination of synthetic parameters represents 1344 unique crystallization reactions (Fig. 1b).

To expedite the investigation of this synthetic parameter space, we employed automated HT synthesis techniques. Solvothermal syntheses were performed with a Chemspeed Flex platform equipped with automated tools to deliver reagents, seal sample vials, agitate and heat samples, and monitor reaction progress (Fig. S1). This platform can automate the MOF synthesis process and prepare up to 84 reactions in a single cycle. After transferring the RE, linker, and modulator reagents to each sample vial, the vials are sealed, shaken, and heated at the target temperature for 18 hours. This arbitrary time interval enabled both sample preparation and heating to be completed in a single day. The samples are then removed for characterization and the reagents are restocked for a new cycle. This platform enabled us to complete our RE-MOF exploratory synthesis campaign (1344 reactions) in 18 days, while significantly reducing active researcher time compared to traditional manual materials synthesis.

Identification of product frameworks with high-throughput powder X-ray diffraction

To determine the identity of the product materials, we employed HT-PXRD to identify the crystallographic phases present. Following automated synthesis, solid samples were transferred to a 96-well PXRD plate (Fig. S2). Samples were transferred manually following unsuccessful attempts to optimize automated transfer of powder samples. The plate was mounted onto a diffractometer equipped with a motorized stage to orient each well in the path of the X-ray beam. This enabled sequential measurement of the entire plate without manual intervention to change samples. With this setup, we characterized each sample resulting in solid products from our HT synthesis campaign, measuring a total of 723 PXRD patterns (Fig. S3–S26).

We aimed to use this bulk characterization data to identify the major crystalline products in each sample. However, direct structural determination from PXRD data is challenging, as it relies on the researcher's expertise to ensure the proposed structure model is crystallographically and chemically reasonable.[39–41] This makes the automated classification of PXRD data particularly difficult in a HT context.[42] While progress has been made towards developing increasingly automated PXRD classification and structure determination tools,[43–46] limitations remain for exploratory synthesis campaigns where the identity and crystallinity of the products are unknown. Automated structure determination tools may require an initial structure model and are commonly developed for specific classes of materials using simulated PXRD data free of noise, peak broadening, or other artifacts that adversely affect performance.[47] RE-MOFs present additional challenges: in addition to the potential for mixtures of multiple crystalline phases, RE ions with different ionic radii can form isostructural analogues to reported framework structures that differ slightly in their unit cell parameters, resulting in the same diffraction patterns with slightly shifted 2θ peak positions.[48]

With these challenges in mind, we sought to develop a HT screening tool to aid in the identification of major product phases from reported structures, as opposed to refining individual structure models for each experimental pattern. Our goal was to differentiate between samples corresponding to known crystal structures and samples that are potentially unreported frameworks in need of further characterization. The experimental powder dataset was compared against simulated powder patterns generated from published crystal structures in the Cambridge Structural Database (CSD).[49,50] To avoid searching against over a million structures in the complete CSD, we identified structures containing both the linker of interest and any lanthanide metal to construct smaller libraries of potential products (ranging from 9–168 structures, depending on the identity of the linker; see SI Section 4.2).

Simulated PXRD patterns were generated from these reported structures, yielding position-intensity lists of each peak in the reference powder patterns. Analogous position-intensity lists were generated from experimental PXRD patterns. For each experimental peaklist, reference peaklists were interpreted to identify likely pairs of matching peak positions using a Gaussian function (eqn S1). The intensities of these matched experimental-reference peak pairs were then compared in order to calculate a similarity score for each reference pattern (eqn S2). These scores were used to expedite the classification of each powder pattern and identify samples representing previously unreported structures. The complete HT search-match screening script is available in our GitHub repository (https://github.com/farhagroupnu/pxrd-CSD-search-match) and described in detail in Section 4 of the SI. The following section provides illustrative examples of experimental PXRD classification to demonstrate the practical implementation of this screening tool.

As a representative example, we first detail our PXRD phase classification workflow for samples crystallized with trimellitic acid (H_3trimel) as a linker. Simple visual inspection of experimental PXRD data (Fig. 2a) indicates the presence of at least three crystallographic phases over the range of REs. HT search-match screening revealed the light REs (including La, Ce, Pr, and Nd) form the reported MIL-81 framework (RE(trimel)(H_2O), Fig. 2b).[51] This structure is identified by the CSD refcode *UTONAT*, which shows good agreement in peak positions and intensities between the experimental data and simulated reference pattern (Fig. S27). MIL-81 is a 3D framework with 9-coordinated RE ion chain nodes, each coordinated by two bidentate carboxylate ligands, four monodentate carboxylate ligands, and one water molecule (Fig. S34). Intermediate REs (including Gd, Tb, Dy, and Ho) form a separate 3D MOF with formula [RE(trimel)(H_2O)$_3$]. This framework also has 9-coordinated ion nodes, with each RE ion coordinated by two bidentate carboxylate ligands, two monodentate carboxylate ligands, and three water molecules (Fig. S35). We note three matched reference structures in the CSD that have the same space group, framework coordination and topology, and similar unit cell parameters (Table S3), but differ in the identity of the RE ion reported: *SEVWEV* (Nd),[52] *ROWZEM* (Eu),[53] and *VOYWUB* (Er).[54] Accordingly, our HT search-match screening identifies multiple high-agreement structures for these experimental samples (Fig. S28). For heavy lanthanides such as Yb and Lu, we identified a third product phase as MIL-92 (RE$_2$(trimel)(H_2O)$_2$, CSD refcode *PEFBEI*).[55] Each RE ion node in this 2D framework is 6-coordinated by one bidentate carboxylate linker, two monodentate carboxylate linkers, and two water molecules (Fig. S36).

Rather than discrete boundaries between the different framework products, mixtures of multiple phases are frequently observed for reactions with REs bordering two crystallographic phases. These samples are identified by our HT search-match screening based on the presence of residual peaks that are unmatched by the top reference structure. These extra peaks

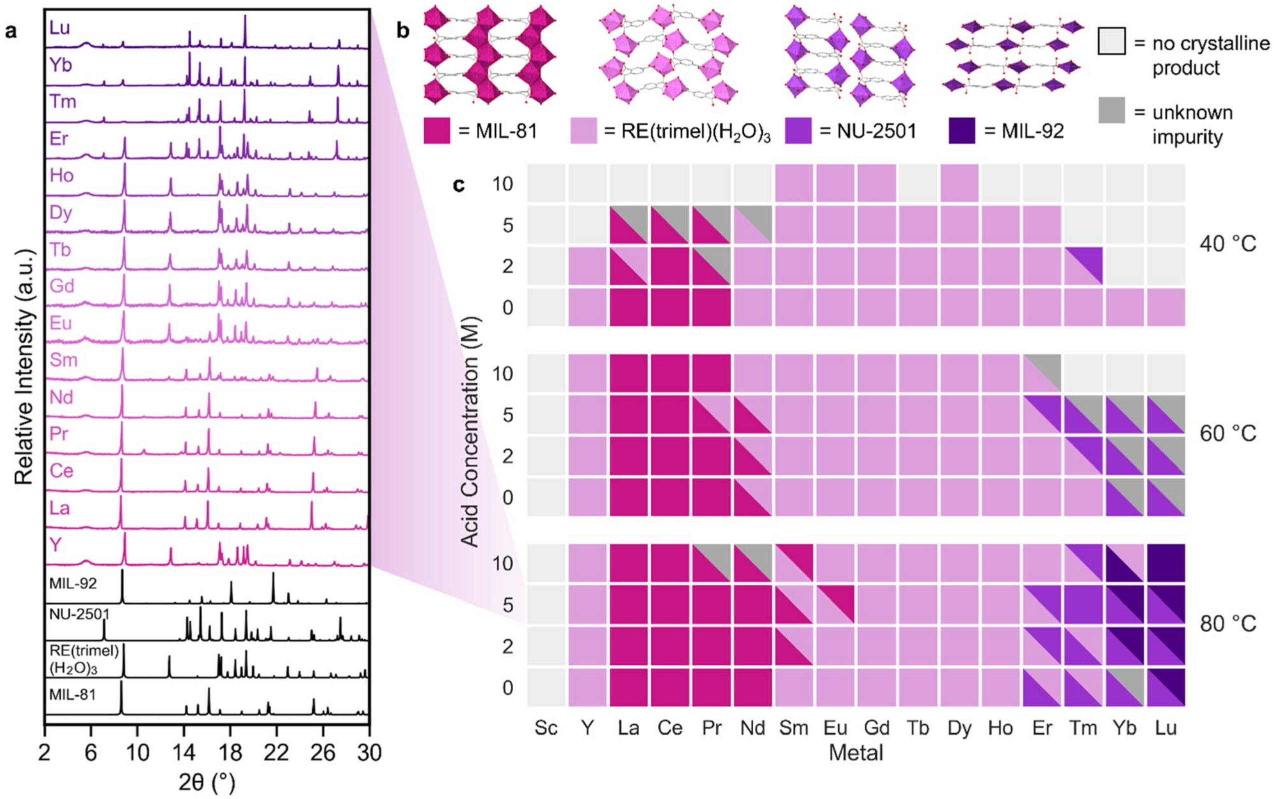

Fig. 2 (a) Normalized PXRD patterns collected of products obtained from crystallization of rare earth metals with trimellitic acid linker (H_3trimel) and 5 M acetic acid at 80 °C. Black traces are simulated patterns for the four product phases. (b) Crystalline phases identified from PXRD data. MIL-81, RE(trimel)(H_2O)$_3$, and MIL-92 are previously reported frameworks, while NU-2501 is a new structure. (c) Phase diagram showing framework formation as a function of metal identity, acetic acid concentration, and temperature. Tile colors indicate phases identified by PXRD. Split tiles denote phase mixtures, light gray tiles indicate amorphous samples, and dark gray tiles indicate unidentified impurities.

indicate a potential phase mixture, and a second round of search-matching is initiated for the unmatched peaks to suggest a possible secondary phase. For instance, the crystallization reaction of Nd, trimellitic acid, and 5 M acetic acid at 60 °C produces a mixed-phase sample containing both MIL-81 and [RE(trimel)(H_2O)$_3$] products, as identified through two consecutive rounds of search-matching (Fig. S29).

Following the identification of experimental samples corresponding to reported structures, we turned to samples that were not successfully matched. As an example, for the reaction of Tm, trimellitic acid, and 5 M acetic acid at 80 °C, no reasonable reference structure match was found (Fig. S30), as indicated by poor agreement between the peak positions and intensities of experimental data with the reference structures, and their correspondingly low scores. The lack of a reference structure match suggested that this sample may represent a potentially unreported phase. Indeed, further characterization by SCXRD revealed that this reaction produces a new structure, NU-2501, [RE(trimel)(H_2O)$_3$], which crystallizes in the monoclinic $P2_1/c$ space group (Fig. S52a, S53 and Table S9). This 2D framework consists of columns of RE chain nodes assembled through H-bond interactions. Each node is 8-coordinated by one bidentate carboxylate ligand, three monodentate carboxylate ligands, and three water molecules (Fig. S37).

Our HT search-match screening approach enabled the expedited classification of our experimental PXRD data through the suggestion of likely reference structures and the identification of possible phase mixtures and previously unreported MOFs. Following the assignment of primary and secondary products for each sample, we constructed a phase diagram for the 192 total crystallization reactions performed with trimellitic acid (Fig. 2c). Across the range of REs, we note a preference for distinct phases for large, intermediate, and small ions, as observed in previous RE MOF crystallization studies.[56–58] In addition to the four MOF products described above, 32 samples did not produce crystalline products, including all reactions with Sc and many reactions with increased acetic acid concentrations at 40 °C. We also note the presence of minor crystalline impurities in some samples (see Fig. S31 for a representative example) which could not be identified through our search-match screening or subsequent characterization attempts. A minority of PXRD patterns from our campaign displayed preferred orientation effects from crystallite stacking or large crystal size, complicating automated classification. Manual characterization techniques were strategically used to elucidate the phase of these samples (see discussion in SI Sections 4.7 and 4.8).

Comparison of the resulting products as synthetic conditions change provides insights into the thermodynamic preferences of trimellitic acid framework crystallization. For instance, the MIL-92 framework is observed only with Yb and Lu, and only at 80 °C. As the reaction temperature decreases to 60 °C, NU-2501 is observed as the primary phase for the heavy REs. At 40 °C, no products are observed for Yb and Lu when any quantity of acid modulator is present, indicating that the crystallization of either framework is not accessible at these conditions. A similar phenomenon is observed with light REs with the MIL-81 phase, which does not form any crystalline products at the highest acid concentration at 40 °C.

We applied our HT search-match screening approach to identify product structures corresponding to samples crystallized with trimesic acid, pyromellitic acid, and mellitic acid linkers (Fig. 3). We did not observe solid products for samples crystallized with the ditopic linkers (terephthalic acid, phthalic acid, and isophthalic acid) and therefore did not collect PXRD for these samples. For trimesic acid (H_3btc), we identified two previously reported phases. The first is RE(btc)$(H_2O)_6$, a 2D framework with a stacked sheet structure assembled from 9-coordinated RE ion nodes (Fig. S38). Our search-match screening identified four isostructural versions of this framework, corresponding to CSD refcodes *KEBSOA* (La),[59] *YIMRIL* (Ce),[60] *RAVJUV* (Gd),[61] and *CAQFEI* (Tb)[62] (Table S4). This phase dominates the trimesic acid phase diagram (Fig. S58) and is accessible for REs La through Ho at all temperatures and acid concentrations studied. We observed a second reported phase for heavy REs Tb through Lu: MIL-78 (RE_2(btc)), identified by CSD refcode *BEVSUR*.[63] MIL-78 is a 3D framework with 8-coordinated RE ion nodes (Fig. S39). This product is favored at higher synthesis temperatures and is not observed at 60 or 40 °C.

Following the assignment of these reported structures, we turned to the remaining unmatched samples. Reactions of trimesic acid and Sc produced a new crystalline phase distinct

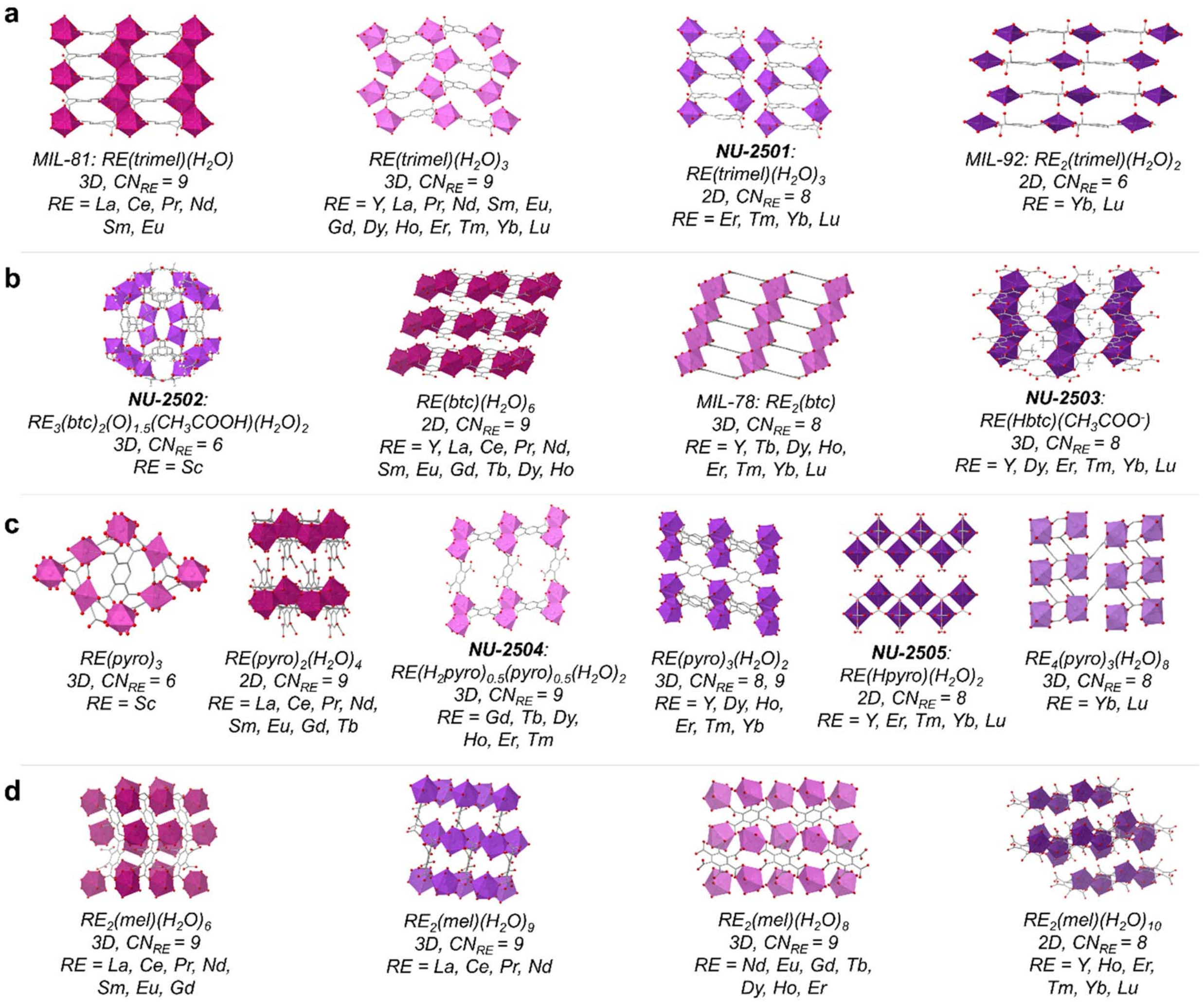

Fig. 3 Crystalline products identified from high-throughput RE-MOF exploratory synthesis campaign, resulting from crystallization reactions with (a) trimellitic acid (H_3trimel), (b) trimesic acid (H_3btc), (c) pyromellitic acid (H_4pyro), and (d) mellitic acid (H_6mel). The dimensionality of the framework, the coordination number (CN) of the RE ions, and the REs observed to form each product are noted under each structure. Bolded structure names indicate previously unreported frameworks. Color code: RE (pink/purple), C (gray), and O (red). Hydrogen atoms are omitted from the structures for clarity.

from previously reported structures, as confirmed by PXRD (Fig. S4). Using SCXRD, we identified this phase as NU-2502, [$Sc_3(btc)_2(O)_{1.5}(CH_3COOH)(H_2O)_2$], which crystallizes in the trigonal $R\bar{3}m$ space group (Fig. S52b, S54 and Table S9). NU-2502 is a 3D framework built upon Sc_2 dimer nodes (Fig. S40). Each Sc ion is coordinated by two monodentate carboxylate ligands and one acetate molecule; the dimer building unit is completed by an oxo bridge and two bridging carboxylate groups from two additional ligands spanning both Sc ions.

We subsequently observed a second unreported MOF resulting from reactions between trimesic acid and heavy REs with 10 M acetic acid. However, attempts at structural characterization with SCXRD proved challenging due to the lack of single crystals with suitable size and quality. To circumvent this limitation, we leveraged MicroED to determine the structure directly from the available microcrystalline powder. This analysis elucidated the structure of NU-2503, [$RE(Hbtc)(CH_3COO^-)$], which crystallizes in the monoclinic $P2_1/c$ space group (Table S9 and Fig. S55). NU-2503 is a 3D framework with 8-coordinated RE ions linked by acetate molecules to form chain nodes throughout the structure (Fig. S41).

Finally, we identified 7 reactions with the trimesic acid linker that resulted in crystalline products, but the PXRD patterns did not demonstrate good agreement with any of the four aforementioned frameworks (see Fig. S32 for a representative example). After unsuccessful attempts to characterize these structures through SCXRD and MicroED, we designated these products of these reactions as an "unknown phase" (Fig. S58).

From the linkers in this campaign, reactions with the tetratopic pyromellitic acid (H_4pyro) linker resulted in the greatest product framework diversity: we observed six distinct phases across the RE series (Fig. S59). For reactions with Sc at 80 °C, we identified a reported structure with CSD refcode *DEJJEK*, a 3D framework featuring 6-coordinated Sc ion nodes (Fig. S42).[64] For light to intermediate REs across all three temperatures, the dominant product was identified as refcode *RIVSOH*, corresponding to $RE(pyro)_2(H_2O)_4$, a layered, 2D framework comprised of 9-coordinated RE nodes (Fig. S43).[65] Moving to the heavy REs (Dy–Yb) at 60 and 80 °C, we observed a third product, the 3D framework [$RE(pyro)_3(H_2O)_2$] (Fig. S44). Two isostructural analogues of this product are published under refcodes *UZATAR*[66] and *MITGOL* (Table S5).[67] Finally, a fourth reported structure was identified in reactions with Yb and Lu at 80 °C, the 3D framework [$RE_4(pyro)_3(H_2O)_8$] corresponding to refcode *MITGIF* (Fig. S45).[67]

SCXRD analysis revealed two previously unreported pyromellitic acid frameworks, NU-2504 and NU-2505. NU-2504 [$RE(H_2pyro)_{0.5}(pyro)_{0.5}(H_2O)_2$] crystallizes in the triclinic $P\bar{1}$ space group (Fig. S52c, S56 and Table S9). Its architecture is built upon dinuclear RE_2 nodes; with each RE_2 pair coordinated by three fully deprotonated and three half deprotonated bidentate carboxylate ligands, four water molecules, and two bridging carboxylate groups. This assembly creates a 3D framework featuring distinct channels along the *a*-axis (Fig. S46). We found that NU-2504 is accessible at all temperatures for the mid-to heavy-REs (Gd–Tm), frequently appearing as a mixed phase alongside the known $RE(pyro)_3(H_2O)_2$ structure. For the heaviest REs (Yb, Lu) at lower temperatures, the favored product shifts to NU-2505, [($RE(Hpyro)(H_2O)_2$]. Unlike the 3D connectivity of NU-2504, this material crystallizes in the orthorhombic *Pbcm* space group (Fig. S52d, S57 and Table S9) as a 2D framework containing stacked layers assembled from 8-coordinated RE ion nodes (Fig. S47).

For the hexatopic mellitic acid (H_6mel) linker, we identified four product phases, all of which are previously reported (Fig. S60). Light REs were observed to form one of two frameworks. These are [$RE_2(mel)(H_2O)_6$] (Fig. S48) for which we noted 6 isostructures from the CSD[68–72] (Table S6), and [$RE_2(mel)(H_2O)_9$][73] (Fig. S49), both of which are 3D frameworks with 9-coordinated RE ion nodes. Intermediate REs formed a third 3D framework, [$RE_2(mel)(H_2O)_8$] (Fig. S50), accessible across all temperatures and acid concentrations studied. We identified ten matched isostructural analogues for this product (Table S7).[74–78] For heavy REs at 60 °C, the fourth product, [$RE_2(mel)(H_2O)_{10}$], was dominant. This 2D framework is constructed from 8-connected RE ion nodes (Fig. S51) and corresponds to three analogous matched structures (Table S8).[78–80]

Overall, we observed 18 distinct crystallographic product phases across our HT RE-MOF synthesis campaign, including 5 previously unreported structures. Aided by our HT PXRD search-match screening tool, we rapidly identified published framework structures from the CSD and allocated manual characterization resources towards potentially new MOFs. The resulting phase diagrams elucidate which crystallographic phases are thermodynamically accessible under different reaction conditions, and which conditions are ideal for the synthesis of specific phase pure samples.

Determination of crystallization kinetics with computer vision

To complement the thermodynamic insights gained from our product phase diagrams, we sought to probe into the kinetics of each crystallization reaction. While measurements such as *in situ* PXRD would enable precise monitoring of crystalline product formation, the required sample preparation and cost were not feasible for a HT campaign. Instead, we opted to replicate a common practice among experimental materials chemists: simply looking at a sample vial to assess whether solid products have formed. To adapt this action for automated materials discovery, we installed a camera within our synthesis platform to capture images of sample vials over time as the crystallization reactions progressed. Initially, the solutions of metal salts, linkers, and modulators are clear. As frameworks gradually precipitate, the solution becomes cloudy, or solid powder or crystals can be observed collecting at the bottom of the vial. We documented this process by capturing nine images of each vial over the 18-hours synthesis, resulting in a dataset of over 12 000 unique images.

To automate the analysis of these images, we developed a machine-learning-based CV workflow to identify chemically relevant artifacts including solid precipitates and clear or cloudy liquid. Our CV pipeline consists of two consecutive object detection models: the first detects the region of the image corresponding to the sample vial, and the second detects chemical phases within the sample vial region (Fig. S61). These models were trained on a dataset of images captured within our automated synthesis platform and manually annotated by experimental MOF chemists.[81] The phase classification model detects five key chemical phases (Fig. S62): the empty headspace in the vial is classified as either "empty" or "residue," the liquid phases are classified as "clear/homogeneous liquid" or "cloudy/heterogeneous liquid," and solid powder or crystals are identified as "solid." Additional details on our CV workflow are found in Section 5 of the SI, and a thorough discussion of dataset generation, model training and performance, and a comparison to human researchers can be found in our recent tutorial article.[82]

In this study, we focus on the identification of cloudy liquid and solid phases as indicators of MOF formation. Using our CV workflow, we analyzed the time series of images for each sample vial to pinpoint the first appearance of either cloudy liquid or solid material. This timepoint indicates the onset of MOF formation and provides a window into the crystallization kinetics of each sample. Some samples crystallize rapidly, with cloudy liquid and solid classes detected shortly after the start of synthesis (Fig. 4a). In contrast, other samples exhibit slower kinetics, with cloudy liquid and solid phases not appearing until multiple hours of heating time have elapsed (Fig. 4b).

Using CV to analyze each sample image time series enabled us to rapidly identify the onset of crystallization without researcher intervention or manual handling of each sample vial. Based on the detected precipitation time, we categorized the formation rate of each sample as fast (occurring within 1 hour and 45 minutes), moderate (1.75–7 hours), or slow (>7 hours). We plot the resulting crystallization onset time data as a kinetic diagram to examine the influence of reaction conditions on the formation rate of reactions performed with trimellitic acid as a linker (Fig. 5). As expected, decreasing reaction temperature results in slower product formation, and increasing the concentration of acid modulator similarly suppresses the onset of crystallization. For instance, regardless of RE identity, all reactions without an acid modulator at 80 °C exhibit fast crystallization. When the acid concentration is increased to 10 M and the temperature is decreased to 40 °C, the majority of REs demonstrate slow product formation. We also note a general trend of faster formation rates for light REs compared to heavy

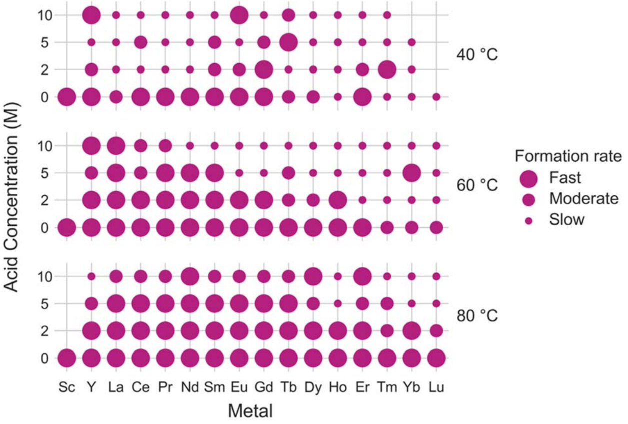

Fig. 5 Kinetic diagram of product formation onset times for reactions with trimellitic acid linker. The size of the marker indicates product formation rate: fast (<1.75 hours), moderate (1.75–7 hours), or slow (>7 hours). The absence of a marker indicates a reaction where no products were observed.

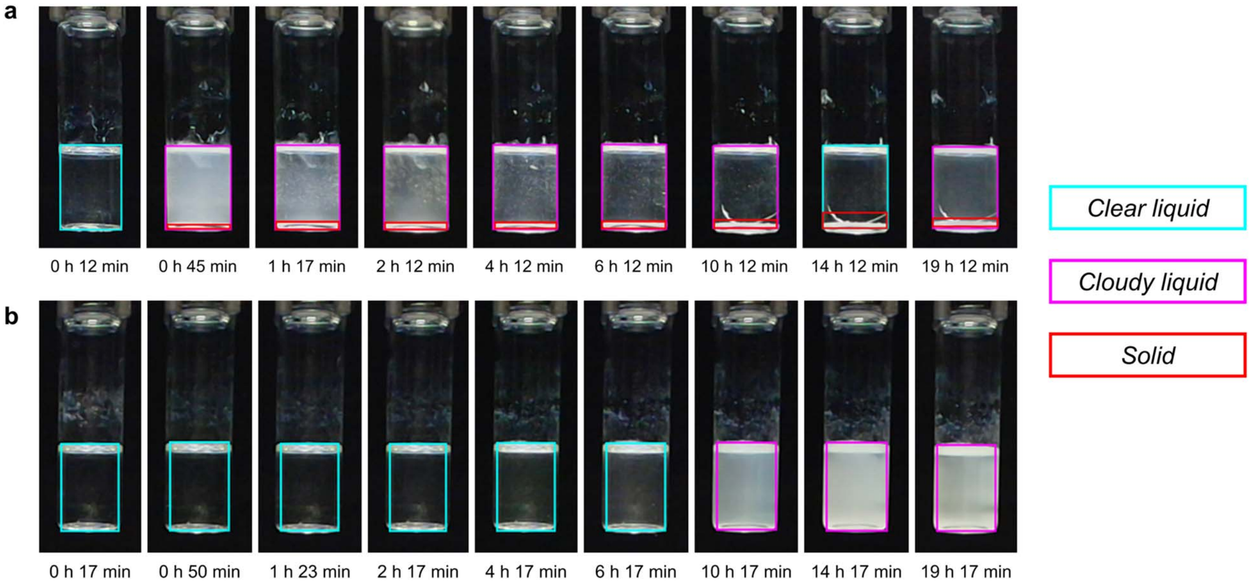

Fig. 4 Determination of product formation rate through computer vision-based analysis of images captured during MOF synthesis reactions. Overlaid boxes indicate the regions of each image corresponding to clear liquid (blue), cloudy liquid (purple), and solid (red), as detected by our CV model. Time series (a) depicts a representative "fast" crystallization reaction (Y, trimellitic acid, 0 M acetic acid, 80 °C), where cloudy liquid and solid phases are detected after 45 minutes. Time series (b) depicts a representative "slow" crystallization reaction (Pr, trimellitic acid, 5 M acetic acid, 40 °C), where cloudy liquid is detected after 10 hours, indicating the onset of MOF precipitation.

REs. The interplay between modulator concentration and RE identity is particularly evident in trimellitic acid samples synthesized at 60 °C. As the modulator concentration increases from 0 to 10 M, the proportion of REs with fast formation rates gradually decreases. At 0 M, Sc, Y, and lanthanides La through Er have fast kinetics, while at 10 M, only Y and La retain this fast formation rate, with lanthanides Nd through Lu exhibiting slow product formation.

We observe similar trends in product formation onset times for samples synthesized with pyromellitic acid as a linker (Fig. S63). At higher temperatures and lower modulator concentrations, fast crystallization is observed, with light REs generally exhibiting faster formation rates than heavy REs. For reactions at 80 °C with no modulator, all 14 lanthanides exhibit fast formation rates, compared to only La through Nd for reactions at 60 °C and 10 M acetic acid. For samples synthesized with trimesic acid, we observe fast product formation rates for all reactions with light REs, regardless of temperature or modulator concentration; only lanthanides heavier than Gd exhibit slow crystallization (Fig. S64). Finally, the hexatopic mellitic acid linker enabled rapid coordination and framework crystallization. Every reaction condition explored with this linker resulted in fast product formation (Fig. S65). Even at the lowest temperature and highest acid concentration, expected to result in the slowest crystallization conditions, sample images revealed rapid precipitation and solid product formation (Fig. S66).

When comparing these kinetic diagrams with thermodynamic preferences for different crystalline MOF phases obtained from our PXRD analysis, we do not observe strong correlations between MOF phase identity and crystallization rate. For instance, samples synthesized with trimellitic acid and 5 M acetic acid at 80 °C, lanthanides La through Tb all exhibit a fast product formation rate (), with lanthanides heavier than Tb displaying moderate or slow crystallization. However, examination of the PXRD phase diagram for these samples (Fig. 2c) reveals that Tb and the next two heavier lanthanides, Dy and Ho, all form the same product, RE(trimel)$(H_2O)_3$, as their primary phase. Similar examples are observed for the other reaction conditions and linkers. While certain phases are generally observed to form more slowly or more quickly, the boundaries between different crystalline products on our phase diagram do not dictate dramatic changes in product formation kinetics. While these formation rates can be tuned based on the reaction temperature and acid concentration, the overall trend of faster crystallization for lighter REs is preserved. Lanthanide identity and ionic radius are therefore more important in governing kinetics than the actual identity of the structure that is ultimately crystallized.

Binary metal crystallization reactions

Building upon our insights into RE-MOF crystallization thermodynamics and kinetics gleaned from PXRD and CV analysis,

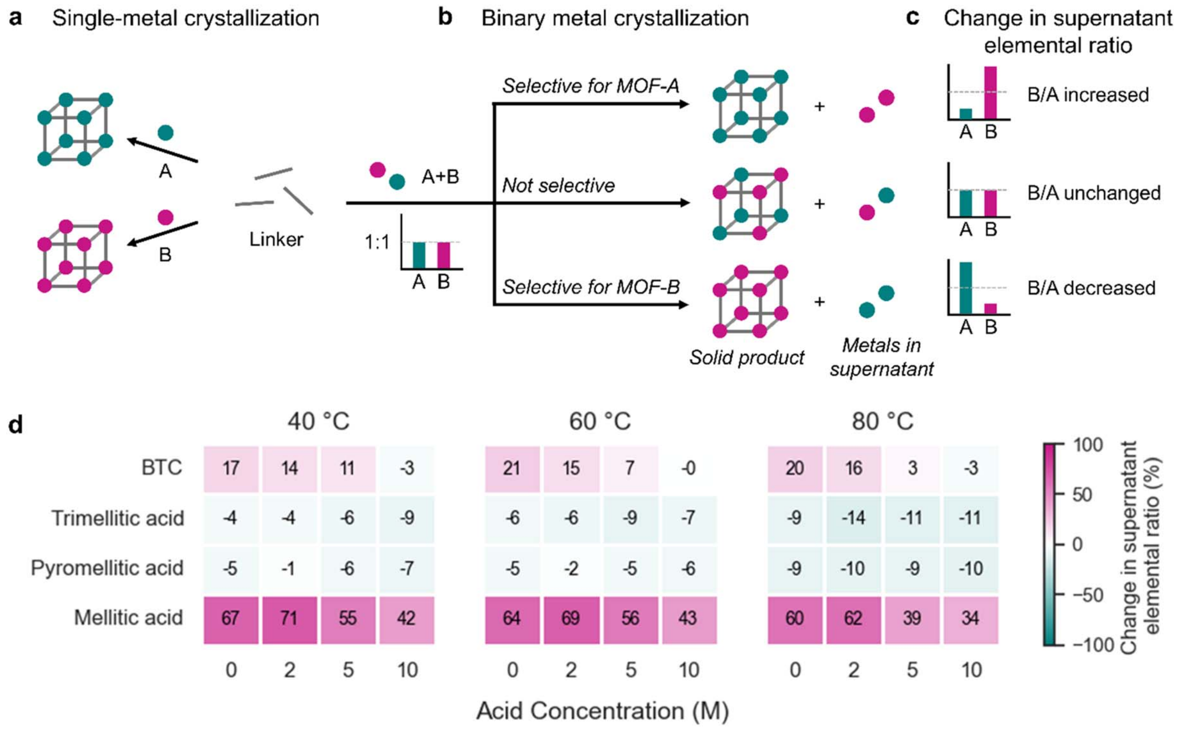

Fig. 6 Scheme depicting (a) crystallization of distinct framework products from a single metal at a time. Binary metal crystallization reactions (b) may display selectivity for either of the MOF products, leaving the non-crystallized ion remaining in the supernatant solution. For reactions with no crystallization selectivity, a mixed-metal product is produced. Comparing the initial ratio of metals to the final ratio in the supernatant solution (c) enables the determination of crystallization selectivity. (d) Percent change in the supernatant elemental ratio compared to the initial 1 : 1 ratio for samples crystallized with a binary mixture of La and Lu. Pink tiles indicate an increased Lu/La ratio in the supernatant, white tiles indicate no change from the initial Lu/La ratio, and teal tiles indicate a decreased Lu/La ratio in the supernatant.

we established a proof-of-concept selective crystallization of a single MOF product from an initial mixture of multiple REs.[56,57,83,84] Our single-metal crystallization trials outlined the landscape of potential crystalline products for a given set of synthetic conditions (Fig. 6a). Applying these conditions to a reaction with two REs present could result in multiple possible products, including either of the single-metal frameworks, a physical mixture of both, or frameworks with both metals incorporated into the same structure (Fig. 6b). The optimal selective crystallization reaction would sequester a single RE into the MOF lattice, yielding a solid product that is easily separable from the non-crystallized RE remaining in solution. This would enable a heterogeneous separation strategy with milder reaction conditions than are typically employed in traditional homogeneous RE purification approaches.[37,85,86] Therefore, our goal was to rapidly identify which synthetic conditions resulted in the greatest crystallization selectivity.

To probe the crystallization selectivity for light *vs.* heavy REs, we performed binary crystallization trials with a 1 : 1 molar ratio mixture of La and Lu. We surveyed the same acid concentrations, temperatures, and four linkers resulting in crystalline MOFs from our single metal synthesis campaign. Based on the results from our CV kinetic analysis, which revealed faster product formation rates for light RE-MOFs, we reduced the reaction time to one hour. We hypothesized that a shorter reaction time could increase crystallization selectivity by preventing significant amounts of the slower-forming heavy RE-MOF products from forming. Following the reaction, we characterized the solid products with HT-PXRD (Fig. S67–S70).

For samples synthesized with trimesic acid as a linker, all reaction conditions resulted in PXRD patterns consistent with $RE(btc)(H_2O)_6$ (Fig. S67), which is the product from the corresponding single metal synthesis with La. For trimellitic acid, pyromellitic acid, and mellitic acid, we observed generally lower crystallinity (lower peak intensities relative to background) for samples synthesized in these rapid binary metal reactions compared to our single metal campaign. Given the short reaction duration, these samples seem to be in the early stages of framework assembly. Therefore, we did not observe highly crystalline products for samples with these linkers crystallized at 40 and 60 °C. At 80 °C, we observe the same trend for the preferential synthesis of the La (light RE) phase: MIL-81 for trimellitic acid, $RE(pyro)_2(H_2O)_4$ for pyromellitic acid, and $RE_2(mel)(H_2O)_6$ for mellitic acid (Fig. S78). We did not identify PXRD patterns consistent with the Lu (heavy RE) product MOFs for any of the linkers studied.

We captured images of each sample at 10-minutes intervals throughout the binary crystallization reactions and constructed a kinetic diagram to visualize the relative product formation rates (Fig. S81). The mellitic acid samples demonstrated the fastest product formation rates, with all reactions displaying cloudy liquid or solid material within 16 minutes. Reactions with BTC as a linker had similarly fast kinetics across all temperatures. In contrast, the pyromellitic acid and trimellitic acid samples had overall slower product formation kinetics, as well as multiple reactions with no solid products produced. The combination of PXRD and CV analysis proved critical for interpreting these binary metal crystallization reactions. For instance, while all reaction conditions with mellitic acid demonstrated fast formation rates by CV, only the 80 °C reactions resulted in crystalline MOF products (Fig. S70). Despite the fast precipitation exhibited in the 40 and 60 °C reactions (representative example shown in Fig. S84), these conditions are not sufficient for ordered self-assembly in such a short duration, producing only non-crystalline products instead.

Quantification of crystallization selectivity with high-throughput X-ray fluorescence

The PXRD patterns confirmed that these binary trials demonstrate a crystallographic preference for the MOF phase corresponding to the lighter RE, La. However, quantifying the reaction selectivity requires determining the elemental composition, as both RE ions can potentially incorporate within the same crystalline lattice. We developed a HT approach using XRF spectroscopy to determine the elemental composition of REs in the reaction supernatant solutions. Comparing the initial elemental ratio in the binary metal stock solution to the final ratio in the reaction supernatant quantifies preferential incorporation (Fig. 6c). For instance, if a MOF containing only La was selectively crystallized from an initial equimolar solution of La and Lu, the final supernatant solution would be expected to contain a Lu : La ratio greater than 1 : 1, as La ions would be removed from the solution to form the solid MOF product. Alternatively, crystallization reactions with poor selectivity, incorporating both La and Lu into the product frameworks, would result in supernatant solutions with relative Lu : La concentrations unchanged. This method of sampling the supernatant enabled facile elemental determination while maintaining compatibility with our automated synthesis platform and bypassing the labor-intensive process of digesting each solid MOF sample.

Following each binary metal crystallization trial, we used automated liquid handling to sample the supernatant by pipetting from the top of the liquid volume within each sample vial. The solution was transferred to filter paper rounds housed in custom XRF sample holders (Fig. S85). Once sample preparation for all vials was complete, the holders were transferred to the XRF spectrometer to determine the molar ratios of the elements present in the supernatant. These final elemental ratios were compared to the initial ratio in the metal stock solution (Lu : La = 1.03) to calculate the percent change in the Lu : La ratio following crystallization (Fig. 6d).

Across all temperatures and acid concentrations for the trimellitic acid and pyromellitic acid linkers, final Lu : La ratios are slightly decreased. However, these values are within 14% of the initial Lu : La ratio, indicating low Lu selectivity in the solid product. In contrast, reactions with mellitic acid exhibit increased Lu : La ratios, corresponding to supernatant solutions enriched in Lu. The greatest change in Lu : La ratio was observed for the reaction of mellitic acid with 2 M acetic acid at 40 °C. For this reaction, the percent change in Lu : La ratio was 71 ± 3%, corresponding to a Lu : La ratio of 1.8 in the supernatant solution (Fig. 6d and Table S10). With BTC as the linker, the greatest change in Lu : La ratio was observed for the reaction performed with no acid modulator at 60 °C, resulting in a percent change in Lu : La ratio of $21 \pm 3\%$, corresponding to a Lu : La ratio of 1.25 in the supernatant (Fig. 5d and Table S10). In addition to binary trials with La + Lu, we also investigated the element pairs La + Gd and Gd + Lu, and performed characterization by PXRD (Fig. S71–S77) and CV image analysis (Fig. S82 and S83). Determinations of the phase identity based on PXRD Fig. S79 and S80) confirmed the formation of crystallographic phases corresponding to the lighter RE of each pair, consistent with our results for La + Lu. XRF analysis of the supernatant solutions for reactions with La + Gd (Fig. S87 and Table S11) demonstrated similar trends as the La + Lu trials, with mellitic acid having the greatest selectivity for La incorporation, followed by BTC. For reactions with Gd + Lu, we did not observe selective incorporation of either RE (Fig. S88 and Table S12).

XRF selectivity measurements in combination with our PXRD results indicate that forming a highly crystalline material is not a prerequisite for the preferential incorporation of one RE over another. In fact, for La + Lu trials, we observe the greatest selectivity for preferential La incorporation for reactions with mellitic acid at 40 and 60 °C, which formed non-crystalline products. These samples demonstrated rapid precipitation based on CV image analysis (Fig. S81), but PXRD measurements revealed the products were amorphous. Assembling an extended framework structure requires reversible coordination between the carboxylate linkers and metal ions to promote error correction and increased crystallinity. The short duration of the binary metal trials (1 hour) was sufficient for rapid precipitation for the mellitic acid samples, but the resulting products demonstrated low to no crystallinity compared to the single-metal reactions, which occurred over a longer duration (18 hours). Despite this, these samples demonstrated a greater Lu : La enrichment in the reaction supernatant, indicating higher selectivity for the preferential incorporation of La. Slowing framework assembly does not enhance selectivity, but instead facilitates the co-incorporation of the disfavored metal. The rate of product formation is therefore crucial for selectivity. This is consistent with the rapid precipitation observed for all single-metal reaction conditions with mellitic acid (Fig. S65). In our binary metal trials, we also observe decreased selectivity for Lu : La in the supernatant as the concentration of acetic acid modulator is increased (Fig. 6). The presence of acidic species that compete with linkers for coordination to metal ions slows the framework assembly process and facilitates the co-incorporation of both REs. Despite the limitations of selective crystallization under these conditions, interpreting our XRF results alongside information gained from our PXRD and CV image analysis provided a more complete picture of these binary metal crystallization trials.

Conclusions

In this study, we demonstrated an automated, high-throughput workflow to expedite exploratory MOF synthesis and characterization, illustrated through a case study focused on RE-carboxylate MOF crystallization. Between our single-metal and binary-metal crystallization trials, we performed a total of 1488 unique MOF synthesis reactions within our automated platform, representing a significant savings of active researcher time compared to manual synthesis approaches. We characterized the bulk structure of these samples using HT-PXRD, collecting a total of 815 patterns, and utilized a custom PXRD screening tool to match experimental data to previously reported MOF structures in the CSD. Through this approach, we identified 18 total framework product phases, mapping the relationship between synthetic conditions and MOF product identity. Manual characterization with SCXRD and MicroED was strategically employed to identify 5 previously unreported MOF structures (NU-2501–NU-2505). To capture crystallization kinetics, we deployed a custom computer vision model to monitor turbidity and precipitation across >13 000 time-resolved images. Furthermore, we developed a HT-XRF workflow to investigate selectivity trends of 144 binary mixtures, identifying mellitic acid to be most effective driver for light-RE separation. The integration of the resulting structural, kinetic, and compositional information provides insights into RE-MOF crystallization that would not have been feasible to obtain with manual characterization approaches. We report the full dataset of reaction outcomes, including unsuccessful syntheses and raw characterization data, to mitigate publication bias and inform future synthetic design. We anticipate combining these automated synthesis and characterization tools with artificial intelligence for sophisticated reaction planning and interpretation will create a powerful platform for future MOF synthesis.[87] While our study focused on RE-MOFs, our HT synthesis and characterization workflow is broadly applicable to the investigation of further classes of materials to optimize synthetic protocols, identify new structures, and uncover thermodynamic and kinetic insights into their formation.

Author contributions

O. K. F. supervised the project; M. A. G. and O. K. F. conceived the project and led the investigation. M. A. G, O. K. F., and K. O. K. designed the experiments and interpreted the results; M. A. G. performed robotic synthesis experiments, conducted HT-PXRD and HT-XRF measurements, collected SCXRD data, developed and conducted PXRD phase matching, and collected and analyzed CV images, with the help of G.-H. K.; C. D. M., N. M. B., and M. A. G. developed HT-PXRD and HT-XRF methods; J. S. M. collected MicroED data; Z.-M. Y., J. S. M., and M. A. G interpreted SCXRD and MicroED data; A. M. and K. D. developed the CV model under the supervision of V. B. and A. A.-G. M. A. G. wrote the manuscript, and all authors reviewed and edited the manuscript.

Conflicts of interest

The authors declare the following competing financial interest: Omar K. Farha has a financial interest in Numat Technologies, a startup company that is seeking to commercialize MOFs. All other authors declare no competing interests.

Data availability

CCDC 2505882–2505886 contain the supplementary crystallographic data for this paper.[88a–e]

The image datasets used to train our CV model are available at https://doi.org/10.5281/zenodo.16209653 and the trained models and analysis scripts are available at https://github.com/AccelerationConsortium/CV-HTE-Tutorial. The HT-PXRD search-match script is available at: https://github.com/farhagroupnu/pxrd-CSD-search-match. The HT-PXRD data, search-match results, CV images and time series figures, and HT-XRF data are https://doi.org/10.5281/zenodo.17902549. Supplementary information (SI): experimental and instrumental details, characterization data, crystallographic and kinetic phase diagrams, and selectivity results. See DOI: https://doi.org/10.1039/d5sc09992g.

Acknowledgements

O. K. F. gratefully acknowledges support from the Underwriters Laboratories' Materials Discovery Research Institute and the Trienens Institute for Sustainability and Energy at Northwestern University. M. A. G. gratefully acknowledges support from the Ryan Fellowship, the International Institute for Nanotechnology (IIN) at Northwestern University, and the International Centre for Diffraction Data (ICDD) through the Ludo Frevel Crystallography Scholarship. This work made use of the IMSERC Crystallography facility at Northwestern University, which has received support from the Soft and Hybrid Nanotechnology Experimental (SHyNE) Resource (NSF ECCS-2025633), and Northwestern University. The purchase and installation of the Rigaku XtaLAB Synergy-ED was made possible by funding from the Air Force Office of Scientific Research (AFOSR) through the Defense University Research Instrumentation Program (grant FA9550-24-1-0058). Metal analysis was performed at the Northwestern University Quantitative Bio-element Imaging Center (QBIC). Computational resources were provided by the Quest High Performance Computing (HPC) facility at Northwestern University, which is jointly supported by the Office of the Provost, the Office for Research, and Northwestern University Information Technology. M. A. G. would like to thank Rebecca Sponenburg for helpful conversations regarding element quantification and Salomon Rodriguez for his kind help fabricating custom hardware components. A. A.-G. thanks the NSERC for the support through the Discovery Grant. A. A.-G. thanks Anders G. Frøseth, for his generous support. A. A.-G. and V. B. also acknowledge support from the Canada 150 Research Chairs program. K. D., A. M., V. B., and A. A.-G. acknowledge critical support from the University of Toronto's Acceleration Consortium, which receives funding from the Canada First Research Excellence Fund (CFREF) *via* CFREF-2022-00042. A. A.-G. and V. B. were supported by the U.S. Department of Energy, Office of Basic Energy Sciences, Division of Chemical Sciences, Geosciences and Biosciences under Award No. DE-SC0023454, as part of the Computational and Theoretical Chemistry Program.

Notes and references

1 S. Sun, N. T. P. Hartono, Z. D. Ren, F. Oviedo, A. M. Buscemi, M. Layurova, D. X. Chen, T. Ogunfunmi, J. Thapa, S. Ramasamy, C. Settens, B. L. DeCost, A. G. Kusne, Z. Liu, S. I. P. Tian, I. M. Peters, J.-P. Correa-Baena and T. Buonassisi, *Joule*, 2019, **3**, 1437–1451.
2 Z. Deng, F. Wei, S. Sun, G. Kieslich, A. K. Cheetham and P. D. Bristowe, *J. Mater. Chem. A*, 2016, **4**, 12025–12029.
3 S. Moradi, S. Kundu, M. Rezazadeh, V. Yeddu, O. Voznyy and M. I. Saidaminov, *Commun. Mater.*, 2022, **3**, 13.
4 S. Matsuda, K. Nishioka and S. Nakanishi, *Sci. Rep.*, 2019, **9**, 6211.
5 T. Adhikari, A. Hebert, M. Adamič, J. Yao, K. Potts and E. McCalla, *ACS Comb. Sci.*, 2020, **22**, 311–318.
6 E. Reddington, A. Sapienza, B. Gurau, R. Viswanathan, S. Sarangapani, E. S. Smotkin and T. E. Mallouk, *Science*, 1998, **280**, 1735–1737.
7 Y. Yao, Z. Huang, T. Li, H. Wang, Y. Liu, H. S. Stein, Y. Mao, J. Gao, M. Jiao, Q. Dong, J. Dai, P. Xie, H. Xie, S. D. Lacey, I. Takeuchi, J. M. Gregoire, R. Jiang, C. Wang, A. D. Taylor, R. Shahbazian-Yassar and L. Hu, *Proc. Natl. Acad. Sci. U. S. A.*, 2020, **117**, 6316–6322.
8 Y. Yang, G. Chen, R. Zeng, A. M. Villarino, F. J. DiSalvo, R. B. van Dover and H. D. Abruña, *J. Am. Chem. Soc.*, 2020, **142**, 3980–3988.
9 H. Furukawa, K. E. Cordova, M. O'Keeffe and O. M. Yaghi, *Science*, 2013, **341**, 1230444.
10 S. M. Moosavi, A. Nandy, K. M. Jablonka, D. Ongari, J. P. Janet, P. G. Boyd, Y. Lee, B. Smit and H. J. Kulik, *Nat. Commun.*, 2020, **11**, 4068.
11 N. Stock and S. Biswas, *Chem. Rev.*, 2012, **112**, 933–969.
12 P. M. Forster, A. R. Burbank, C. Livage, G. Férey and A. K. Cheetham, *Chem. Commun.*, 2004, 368–369, DOI: 10.1039/B311156C.
13 H. H.-M. Yeung and A. K. Cheetham, *Dalton Trans.*, 2014, **43**, 95–102.
14 S. E. Henkelis, D. J. Vogel, P. C. Metz, N. R. Valdez, M. A. Rodriguez, D. X. Rademacher, S. Purdy, S. J. Percival, J. M. Rimsza, K. Page and T. M. Nenoff, *ACS Appl. Mater. Interfaces*, 2021, **13**, 56337–56347.
15 S. L. Hanna, M. Barsoum, T. T. Debela, C. D. Malliakas, M. A. Gaidimas, J. G. Knapp, K. O. Kirlikovali, C. H. Hendon, V. P. Dravid and O. K. Farha, *ACS Mater. Lett.*, 2023, **5**, 2518–2527.
16 S. M. Shaikh, P. M. Usov, J. Zhu, M. Cai, J. Alatis and A. J. Morris, *Inorg. Chem.*, 2019, **58**, 5145–5153.
17 T. Ahnfeldt, N. Guillou, D. Gunzelmann, I. Margiolaki, T. Loiseau, G. Férey, J. Senker and N. Stock, *Angew. Chem., Int. Ed.*, 2009, **48**, 5163–5166.
18 S. Bauer, C. Serre, T. Devic, P. Horcajada, J. Marrot, G. Férey and N. Stock, *Inorg. Chem.*, 2008, **47**, 7568–7576.
19 R. S. Forgan, *Chem. Sci.*, 2020, **11**, 4546–4562.
20 A. Schaate, P. Roy, A. Godt, J. Lippke, F. Waltz, M. Wiebcke and P. Behrens, *Chem.–Eur. J.*, 2011, **17**, 6643–6651.

21 K. Hemmer, H. L. B. Boström, S. Krause, B. V. Lotsch and R. A. Fischer, *Commun. Mater.*, 2024, **5**, 264.

22 Z. Chen, K. O. Kirlikovali, P. Li and O. K. Farha, *Acc. Chem. Res.*, 2022, **55**, 579–591.

23 A. M. Tollitt, R. Vismara, L. M. Daniels, D. Antypov, M. W. Gaultois, A. P. Katsoulidis and M. J. Rosseinsky, *Angew. Chem., Int. Ed.*, 2021, **60**, 26939–26946.

24 M. L. Kelty, W. Morris, A. T. Gallagher, J. S. Anderson, K. A. Brown, C. A. Mirkin and T. D. Harris, *Chem. Commun.*, 2016, **52**, 7854–7857.

25 E. Biemmi, S. Christian, N. Stock and T. Bein, *Microporous Mesoporous Mater.*, 2009, **117**, 111–117.

26 S. M. Moosavi, A. Chidambaram, L. Talirz, M. Haranczyk, K. C. Stylianou and B. Smit, *Nat. Commun.*, 2019, **10**, 539.

27 N. M. Padial, J. Castells-Gil, N. Almora-Barrios, M. Romero-Angel, I. da Silva, M. Barawi, A. García-Sánchez, V. A. de la Peña O'Shea and C. Martí-Gastaldo, *J. Am. Chem. Soc.*, 2019, **141**, 13124–13133.

28 A. Sonnauer, F. Hoffmann, M. Fröba, L. Kienle, V. Duppel, M. Thommes, C. Serre, G. Férey and N. Stock, *Angew. Chem., Int. Ed.*, 2009, **48**, 3791–3794.

29 K. Sumida, S. Horike, S. S. Kaye, Z. R. Herm, W. L. Queen, C. M. Brown, F. Grandjean, G. J. Long, A. Dailly and J. R. Long, *Chem. Sci.*, 2010, **1**, 184–191.

30 R. Banerjee, A. Phan, B. Wang, C. Knobler, H. Furukawa, M. O'Keeffe and O. M. Yaghi, *Science*, 2008, **319**, 939–943.

31 D. He, Y. Jiang, M. Guillén-Soler, Z. Geary, L. Vizcaíno-Anaya, D. Salley, M. D. C. Gimenez-Lopez, D.-L. Long and L. Cronin, *J. Am. Chem. Soc.*, 2024, **146**, 28952–28960.

32 H. Reinsch, M. A. van der Veen, B. Gil, B. Marszalek, T. Verbiest, D. de Vos and N. Stock, *Chem. Mater.*, 2013, **25**, 17–26.

33 X. Gong, K. Gnanasekaran, K. Ma, C. J. Forman, X. Wang, S. Su, O. K. Farha and N. C. Gianneschi, *J. Am. Chem. Soc.*, 2022, **144**, 6674–6680.

34 M. Ge, Y. Wang, F. Carraro, W. Liang, M. Roostaeinia, S. Siahrostami, D. M. Proserpio, C. Doonan, P. Falcaro, H. Zheng, X. Zou and Z. Huang, *Angew. Chem., Int. Ed.*, 2021, **60**, 11391–11397.

35 Y. Luo, B. Wang, S. Smeets, J. Sun, W. Yang and X. Zou, *Nat. Chem.*, 2023, **15**, 483–490.

36 P. Wollmann, M. Leistner, U. Stoeck, R. Grünker, K. Gedrich, N. Klein, O. Throl, W. Grählert, I. Senkovska, F. Dreisbach and S. Kaskel, *Chem. Commun.*, 2011, **47**, 5151–5153.

37 T. Cheisson and E. J. Schelter, *Science*, 2019, **363**, 489–493.

38 F. Saraci, V. Quezada-Novoa, P. R. Donnarumma and A. J. Howarth, *Chem. Soc. Rev.*, 2020, **49**, 7949–7977.

39 B. H. Toby, *Powder Diffr.*, 2006, **21**, 67–70.

40 L. B. McCusker, R. B. Von Dreele, D. E. Cox, D. Louër and P. Scardi, *J. Appl. Crystallogr.*, 1999, **32**, 36–50.

41 N. D. Loh, *Nat. Mater.*, 2025, **24**, 1670–1671.

42 J. Leeman, Y. Liu, J. Stiles, S. B. Lee, P. Bhatt, L. M. Schoop and R. G. Palgrave, *PRX Energy*, 2024, **3**, 011002.

43 J. E. Salgado, S. Lerman, Z. Du, C. Xu and N. Abdolrahim, *npj Comput. Mater.*, 2023, **9**, 214.

44 G. Guo, T. L. Saidi, M. W. Terban, M. Valsecchi, S. J. L. Billinge and H. Lipson, *Nat. Mater.*, 2025, **24**, 1726–1734.

45 L. Chen, B. Wang, W. Zhang, S. Zheng, Z. Chen, M. Zhang, C. Dong, F. Pan and S. Li, *J. Am. Chem. Soc.*, 2024, **146**, 8098–8109.

46 R. A. Mayo, K. M. Marczenko and E. R. Johnson, *Chem. Sci.*, 2023, **14**, 4777–4785.

47 J. Li and J. Sun, *Acc. Chem. Res.*, 2017, **50**, 2737–2745.

48 P. R. Donnarumma, S. Frojmovic, P. Marino, H. A. Bicalho, H. M. Titi and A. J. Howarth, *Chem. Commun.*, 2021, **57**, 6121–6124.

49 C. R. Groom, I. J. Bruno, M. P. Lightfoot and S. C. Ward, *Acta Crystallogr., Sect. B*, 2016, **72**, 171–179.

50 R. A. Sykes, N. T. Johnson, C. J. Kingsbury, J. Harter, A. G. P. Maloney, I. J. Sugden, S. C. Ward, I. J. Bruno, S. A. Adcock, P. A. Wood, P. McCabe, A. A. Moldovan, F. Atkinson, I. Giangreco and J. C. Cole, *J. Appl. Crystallogr.*, 2024, **57**, 1235–1250.

51 S. Surblé, C. Serre, F. Millange and G. Férey, *Solid State Sci.*, 2006, **8**, 413–417.

52 Z.-S. Jin, Z.-B. Duan, G.-C. Wei and J.-Z. Ni, *Chinese J. Struct. Chem.*, 1990, **9**, 69.

53 A. Vardanyan, G. Zhou, N. Kim, T. M. Budnyak, V. G. Kessler, I. S. Choi, Z. Huang and G. A. Seisenbaeva, *Commun. Mater.*, 2024, **5**, 187.

54 G.-C. Wei, Z.-B. Duan, Z.-S. Jin and J.-Z. Ni, *Chinese J. Struct. Chem.*, 1992, **11**, 96.

55 S. Surblé, C. Serre, F. Millange, F. Pelle and G. Férey, *Solid State Sci.*, 2005, **7**, 1074–1082.

56 H. Ya Gao, W. Li Peng, P. Pan Meng, X. Feng Feng, J. Qiang Li, H. Qiong Wu, C. Sheng Yan, Y. Yang Xiong and F. Luo, *Chem. Commun.*, 2017, **53**, 5737–5739.

57 X. Yin, Y. Wang, Y. Li, X. Jia, J. Sun, H. Lu and Q. Li, *Inorg. Chem.*, 2025, **64**, 5816–5820.

58 N. Sapkota, E. Mäkilä, A. Lehtonen and A. Peuronen, *Cryst. Growth Des.*, 2025, **25**, 3119–3127.

59 Y.-H. Wen, J.-K. Cheng, Y.-L. Feng, J. Zhang, Z.-J. Li and Y.-G. Yao, *Chin. J. Struct. Chem.*, 2005, **24**, 5.

60 H. Jia, B. Yin, J. Chen, Y. Zou, H. Wang, Y. Zhang, T. Ma, Q. Shi, J. Yao, S. Bai and C. Zhang, *Angew. Chem., Int. Ed.*, 2023, **62**, e202309073.

61 K. Davies, S. A. Bourne and C. L. Oliver, *Cryst. Growth Des.*, 2012, **12**, 1999–2003.

62 M. Honjo, T. Koshiyama, Y. Fukunaga, Y. Tsuji, M. Tanaka and M. Ohba, *Dalton Trans.*, 2017, **46**, 7141–7144.

63 C. Serre, F. Millange, C. Thouvenot, N. Gardant, F. Pellé and G. Férey, *J. Mater. Chem.*, 2004, **14**, 1540–1543.

64 A. A. Zakariya and E. Şahin, *CSD Communication*, 2017, DOI: 10.5517/ccdc.csd.cc1pxtcs.

65 L.-W. Lee, S.-Y. Pao, A. Pathak, D.-Y. Kang and K.-L. Lu, *Environ. Sci.: Nano*, 2019, **6**, 1067–1076.

66 S.-M. Li, S.-Y. Niu, J. Jin, Y.-X. Chi, C.-X. Lu, W.-T. Zhu, Y. Li and G.-N. Zhang, *Wuji Huaxue Xuebao*, 2011, **27**, 1697.

67 R. Cao, D. Sun, Y. Liang, M. Hong, K. Tatsumi and Q. Shi, *Inorg. Chem.*, 2002, **41**, 2087–2094.

68 Y. Han, L. Fu, L. Mafra and F.-N. Shi, *J. Solid State Chem.*, 2012, **186**, 165–170.
69 X. Tang, S. Yue, P. Li, N. Wang and Y. Liu, *J. Rare Earths*, 2008, **26**, 800–803.
70 S. S. Y. Chui, A. Siu, X. Feng, Z. Ying Zhang, T. C. W. Mak and I. D. Williams, *Inorg. Chem. Commun.*, 2001, **4**, 467–470.
71 M. O. Rodrigues, F. A. A. Paz, R. O. Freire, G. F. de Sá, A. Galembeck, M. C. B. S. M. Montenegro, A. N. Araújo and S. Alves Jr, *J. Phys. Chem. B*, 2009, **113**, 12181–12188.
72 C. Volkringer, N. Henry, S. Grandjean and T. Loiseau, *J. Am. Chem. Soc.*, 2012, **134**, 1275–1283.
73 L. P. Wu, M. Munakata, M. Yamamoto, T. Kuroda-Sowa and M. Maekawa, *J. Coord. Chem.*, 1996, **37**, 361–369.
74 K. M. L. Taylor, A. Jin and W. Lin, *Angew. Chem., Int. Ed.*, 2008, **47**, 7722–7725.
75 L. L. da Luz, B. F. Lucena Viana, G. C. O. da Silva, C. C. Gatto, A. M. Fontes, M. Malta, I. T. Weber, M. O. Rodrigues and S. A. Júnior, *CrystEngComm*, 2014, **16**, 6914–6918.
76 L. L. da Luz, R. Milani, J. F. Felix, I. R. B. Ribeiro, M. Talhavini, B. A. D. Neto, J. Chojnacki, M. O. Rodrigues and S. A. Júnior, *ACS Appl. Mater. Interfaces*, 2015, **7**, 27115–27123.
77 K. Li, C. Yan, J. Wang, K. Zhu, J. Guo, Y. Zhang, G. Shi, Y. Yin, L. Cheng, L. Sun, Y. Wang, H. Zhang, Y. Sun, J. Yuan, W. Ma, G. Ji, Z. Chai, Y. Wang, X. Ouyang and S. Wang, *Nature*, 2024, **633**, 811–815.
78 W. Liang Ping, M. Munakata, T. Kuroda-Sowa, M. Maekawa and Y. Suenaga, *Inorg. Chim. Acta*, 1996, **249**, 183–189.
79 Z.-F. Li, C.-X. Wang, P. Wang and Q.-H. Zhang, *Acta Crystallogr., Sect. E*, 2006, **62**, m914–m915.
80 C. Robl and S. Hentschel, *Z. Naturforsch. B.*, 1990, **45**, 1499–1502.
81 M. A. Gaidimas, A. Mandal, G.-H. Kim, K. Darvish, S. X. Leong and A. Talekar, *Zenodo*, 2025, DOI: 10.5281/zenodo.16209653.
82 M. A. Gaidimas, A. Mandal, P. Chen, S. X. Leong, G.-H. Kim, A. Talekar, K. O. Kirlikovali, K. Darvish, O. K. Farha, V. Bernales and A. Aspuru-Guzik, *Dig. Discov.*, 2026, **5**, 510–522.
83 M. A. Gaidimas, C. S. Smoljan, Z.-M. Ye, C. L. Stern, C. D. Malliakas, K. O. Kirlikovali and O. K. Farha, *Chem. Sci.*, 2025, **16**, 3895–3903.
84 X. Zhao, M. Wong, C. Mao, T. X. Trieu, J. Zhang, P. Feng and X. Bu, *J. Am. Chem. Soc.*, 2014, **136**, 12572–12575.
85 D. Talan and Q. Huang, *Miner. Eng.*, 2022, **179**, 107430.
86 F. Xie, T. A. Zhang, D. Dreisinger and F. Doyle, *Miner. Eng.*, 2014, **56**, 10–28.
87 M. A. Gaidimas, J. Bai, Y. Kang, K. O. Kirlikovali, V. Bernales, A. Aspuru-Guzik and O. K. Farha, *Chem*, 2026, **12**, 102921.
88 (*a*) CCDC 2505882: Experimental Crystal Structure Determination, 2026, DOI: 10.5517/ccdc.csd.cc2q3kxb; (*b*) CCDC 2505883: Experimental Crystal Structure Determination, 2026, DOI: 10.5517/ccdc.csd.cc2q3kyc; (*c*) CCDC 2505884: Experimental Crystal Structure Determination, 2026, DOI: 10.5517/ccdc.csd.cc2q3kzd; (*d*) CCDC 2505885: Experimental Crystal Structure Determination, 2026, DOI: 10.5517/ccdc.csd.cc2q3l0g; (*e*) CCDC 2505886: Experimental Crystal Structure Determination, 2026, DOI: 10.5517/ccdc.csd.cc2q3l1h.